Atmospheric
Chemistry
and Physics

Open Access

EGU

Supplement of

Upper-tropospheric slightly ice-subsaturated regions: frequency of occurrence and statistical evidence for the appearance of contrail cirrus

Yun Li et al.

Correspondence to: Yun Li (yun.li@fz-juelich.de) and Martina Krämer (m.kraemer@fz-juelich.de)

This Supplement contains an additional table (Table S1) complementing the ML-CIRRUS dataset introduced in Sect. 2, another table (Table S2) listing the in-cloud sampling time with and without the plume detection algorithm complementing Sect. 2.3 and extra figures supporting the interpretation of our results presented in Sect. 3 of the paper. Details about the table and each figure can be found in the corresponding sections of the paper as mentioned in the supplement figure captions.

5

Contents

15

20

25

30

Table S1. Twelve scientific flights from the ML-CIRRUS 2014 campaign that contain a complete dataset of ice cloud parameters are selected for the study of the microphysical properties and occurrences of contrail and natural cirrus. The table is adapted from Table 3 in Voigt et al. (2017). The cloud particle sampling frequency is 1 Hz (max. ~290 m/s) during flights. See Sect. 2.1 in the paper for details.

| Flight Nr.	Date	Mission of single flights	Flight area	Flight hours
1, 2	March 22 a, b	Test flights	Germany	6.00 h
3	March 26	Contrails and contrail cirrus	North Atlantic flight corridor	8.50 h
4	March 27	Fronts and warm conveyor belts (WCBs) induced cirrus	Alps, Italy, and Germany	4.75 h
5	March 29	Cirrus induced by dynamics, *e.g.*, fronts, convection, *etc*.	France and Spain	7.50 h
6	April 1	Cirrus, contrail cirrus	Germany	6.58 h
7	April 3	Cirrus from WCBs outflow	Germany	5.25 h
8	April 7	Contrail cirrus	Germany	5.58 h
9	April 10	Contrails and contrail cirrus	Germany	3.25 h
10, 11	April 11 a, b	Cirrus from fronts and WCBs	Great Britain	10.00 h
12	April 13	Cirrus in high pressure system and jet stream	France, Spain, Portugal	3.00 h
			Total flight hours:	60.41 h
			Valid data volume in hours:	48.51 h
			Valid cirrus sampling hours:	14.70 h
			Length of sampled in-cloud space: (max. aircraft speed: ~ 290 m/s)	~ 15000 km

Table S2. In-cloud sampling time (at 1 Hz frequency) for different type of clouds after applying the Schmidt-Appleman criterion (SAC[+]), cruising altitude range (CA[+]) and plume detection algorithm. See Sect. 2.3.3 in the paper for details.

Type of clouds	In-cloud time without plume detection	In-cloud time with plume detection
All type of clouds	17.90 h	1.04 h
All cirrus clouds ($T < 235$ K)	14.70 h	0.99 h
Contrail-natural cirrus mixture (SAC[+])	11.18 h	0.86 h
Contrail cirrus (SAC[+], CA[+])	4.01 h	0.35 h

2

S1 In situ-origin contrail cirrus and liquid-origin natural cirrus

In situ-origin cirrus means that the cirrus ice crystals have formed and grown in an ice cloud only environment, while liquid-
origin cirrus refers to the cirrus whose ice crystals originally form as liquid drops in a warmer atmosphere (T_{amb} > 235 K),
which subsequently freeze while being lifted into the cirrus temperature region of the atmosphere. In situ-origin cirrus are
often associated with small ice particles with low ice water content IWC. In contrast, liquid-origin cirrus tends to yield large
ice crystals with higher IWC. See Luebke et al. (2016) and Krämer et al. (2016; 2020) for more details.

From Fig. S1a and b, we can see that the high occurrences of IWC are in the lower IWC range (< 10 parts per million by
volume. 3.99 h (Fig. S1c) out of 4.01 h (Fig. 5a) ice cloud particles are formed in situ. Over two-thirds of the natural cirrus
(Fig. 4b) are liquid-origin cirrus, as shown in Fig. S1c and d, respectively.
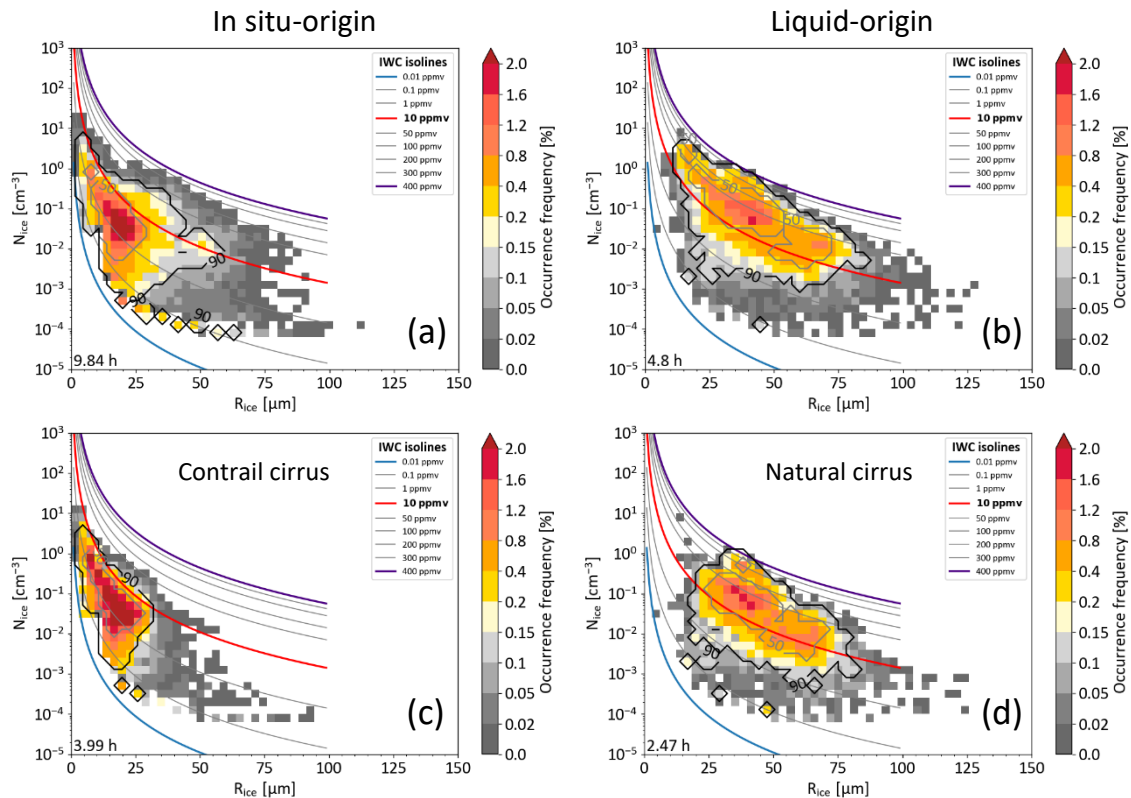
Figure S1. Ice crystal number concentration N_{ice} in relation to mass mean radius R_{ice} for the in situ-origin (left) and liquid-origin cirrus
(right) sampled during the ML-CIRRUS 2014 campaign. Coloured curves in the figures are ice water content IWC isolines in parts per
million by volume (ppmv). The same amount of IWC could consist of many small ice particles pointing to the upper-left end of the isoline
or few large ice crystals in the lower-right end. The size of each dataset in flight hours at 1 Hz sapling frequency is added to the lower right
corner of each figure. The grey and black contours enclose 50% and 90% of the most frequent ice particles. (a): N_{ice}–R_{ice} relation for all in
situ-origin cirrus (medians R_{ice} = 0.03 cm^{-3}, N_{ice} = 20 µm). (b): N_{ice}–R_{ice} relation for all liquid-origin cirrus (medians R_{ice} = 0.05 cm^{-3}, N_{ice} =
42 µm). (c): N_{ice}–R_{ice} relation for all contrail cirrus of in situ-origin (medians: R_{ice} = 0.04 cm^{-3}, N_{ice} = 17 µm). The contrail cirrus is identified
with the Schmidt-Appleman criterion (SAC) and the frequent aircraft cruising altitude range (CA, ambient pressure 200–245 hPa). (d): N_{ice}–
R_{ice} relation for all natural cirrus of liquid-origin (medians: R_{ice} = 0.02 cm^{-3}, N_{ice} = 45 µm). The natural cirrus does not fulfil SAC and CA.
See Sect. 3.1 in the paper for details.

## S2 Slight ice-subsaturation in contrail cirrus

Contrail cirrus is identified by combining the Schmidt-Appleman criterion (SAC, calculated using water vapour emission index, aircraft fuel properties and engine efficiency, see text and Schumann (1996) and the most frequent aircraft cruising altitude range (CA, ambient pressure range 200–245 hPa, ambient temperature range 207–218 K). Contrail cirrus fulfilling SAC and located inside the CA range are shown in Fig. S2b, while natural cirrus missing SAC and CA are shown in Fig. S2c. The color coding shows the relative humidity with respect to ice RH_{ice} in cirrus clouds, revealing that contrail cirrus are mostly subsaturated with respect to ice, with the RH_{ice} around 90% in the area of mass mean radius $R_{ice} < 20$ µm and ice crystal number concentration $N_{ice} > 0.05$ cm^{-3}. High RH_{ice} is more frequently found in the thin in situ-origin cirrus of which both N_{ice} and IWC are small or in the liquid-origin cirrus of more larger ice crystals and higher IWC.
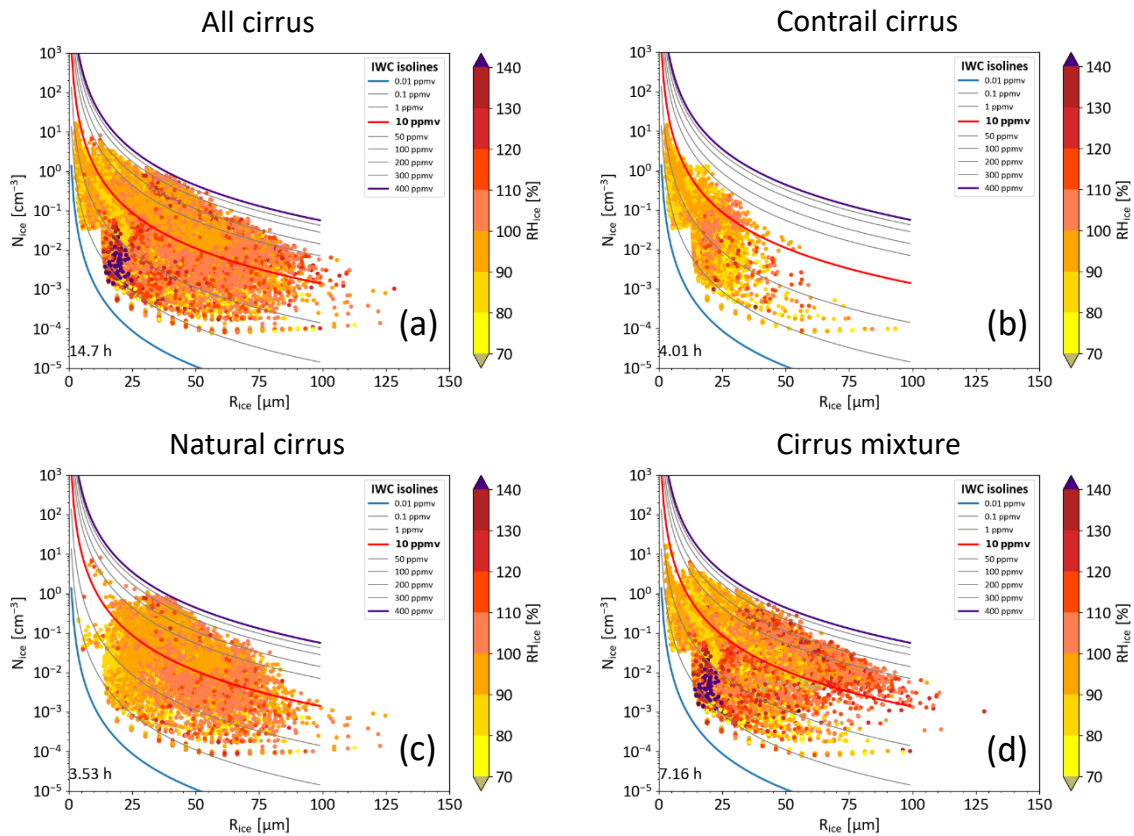
Figure S2. Scatter plots of ice crystal number concentration N_{ice} dependent of mass mean radius R_{ice} in all cirrus clouds (a), the contrail cirrus (b), the natural cirrus (c) and the cirrus mixture (d) sampled during the ML-CIRRUS campaign. Coloured curves in the figures are ice water content IWC isolines in parts per million by volume (ppmv). The same amount of IWC could come from many small ice particles pointing to the upper-left end of the isoline or few large ice crystals in the lower-right end. The size of each dataset in flight hours at 1 Hz sampling frequency is added to the lower left corner of each figure. See Sect. 3.2.1 in the paper for details.

S3 The robustness of the in situ RH$_{ice}$ in relation to the ambient temperature uncertainty

Determination of in situ RH$_{ice}$ values is based on the water vapour measurement of the SHARC hygrometer and the ambient temperature (T$_{amb}$) and pressure measured by the Basis Halo Measurement and Sensor System (BAHAMAS). The nominal accuracies of the BAHAMAS temperature and pressure measurements are 0.3 hPa and 0.5 K, respectively. There could be a small bias in the in situ RH$_{ice}$ dataset due to a positive bias in the measured temperature (T$_{meas}$) by HALO BAHAMAS as indicated in Schumann (2021; See page 108), meaning that the in situ T$_{meas}$ might be slightly warmer than the real T$_{amb}$. To evaluate the changes of in situ RH$_{ice}$ values which could be caused by the temperature uncertainty and to check the robustness of our results, we assume a constant positive bias of 0.5 K in the currently used T$_{meas}$ dataset, *i.e.*, the in situ T$_{meas}$ is constantly 0.5 K warmer than the true T$_{amb}$, and recalculated the saturation pressure over ice at (T$_{meas}$–0.5) K based on Murphy and Koop (2005) and the in situ RH$_{ice}$.
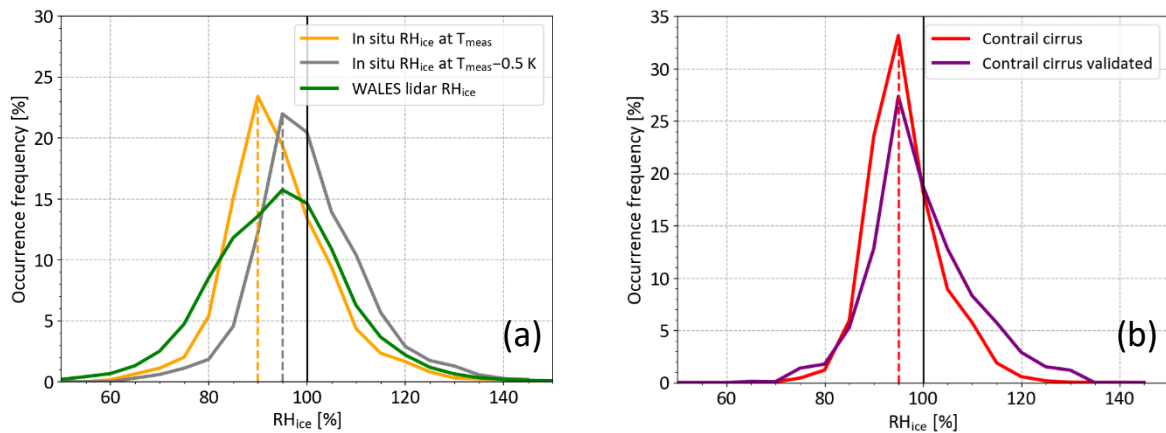
Figure S3. (a): Normalised RH$_{ice}$ occurrence frequency in 5% RH$_{ice}$ bins. The orange curve shows the in situ RH$_{ice}$ distribution with the currently used ambient temperature values T$_{meas}$ provided by the HALO database (https://halo-db.pa.op.dlr.de/). The grey curve exhibits the in situ RH$_{ice}$ distribution with a subtraction of 0.5 K from the currently used temperature values T$_{meas}$. The frequency distribution of the Lidar RH$_{ice}$ measured by the remote sensing instrument WALES on board is shown as the green curve. (b): Normalised RH$_{ice}$ occurrence frequency in 5% RH$_{ice}$ bins with T$_{meas}$ subtracted by 0.5 K for the contrail cirrus (in red) fulfilling the Schmidt-Appleman criterion (SAC) and inside the cruising altitude range (CA) and for the contrail cirrus validated with the plume detection method (fulfilling SAC and the CA range not applied) (in purple). See Sect. 3.3 in the paper for details.

Figure S3a shows the normalised in-cloud RH$_{ice}$ occurrence frequency distribution in all cirrus clouds from the currently used T$_{meas}$ dataset and from the adjusted temperature dataset by subtracting 0.5 K. In addition, the in-cloud RH$_{ice}$ distribution obtained by the lidar WALES is plotted in the figure. We can see, on one hand, that reducing constantly the in situ T$_{meas}$ by 0.5 K makes the peak of the RH$_{ice}$ distribution shift from 90% RH$_{ice}$ under the current T$_{meas}$ dataset to 95% RH$_{ice}$ at slightly colder temperatures, which is at the peak of the lidar RH$_{ice}$. However, when a constant bias is assumed, the whole distribution of RH$_{ice}$ at (T$_{meas}$–0.5) K is shifted rightwards in comparison to the lidar RH$_{ice}$ distribution. The in situ RH$_{ice}$ distribution derived from the current T$_{meas}$ dataset agrees better with the RH$_{ice}$ distribution from the lidar measurements, considering the RH$_{ice}$ ranges at the full width half maxima and the RH$_{ice}$ ranges with the most frequent RH$_{ice}$ occurrence (>80%). Figure S3b displays

5

the normalised frequency distributions of the contrail cirrus (fulfilling SAC and inside CA) and the contrail cirrus that are validated using the plume detection algorithm (fulfilling SAC and CA not applied), at (T_{meas}–0.5) K. The highest occurrence frequency in both contrail cirrus identified using SAC-CA combination and by applying the plume detection method is still in slight ice subsaturation (95%). Concluding, we consider the current T_{meas} dataset, as has been applied in many previous publications, see *e.g.*, the ACP/AMT inter-journal Special Issue: ML-CIRRUS – the airborne experiment on natural cirrus and contrail cirrus in mid-latitudes with the high-altitude long-range research aircraft HALO (https://acp.copernicus.org/articles/special_issue820.html), and specifically Kaufmann et al. (2018); Krämer et al. (2020); Luebke et al. (2016); Schumann et al. (2017); Voigt et al. (2017), as applicable within the specified uncertainties.

S4 Contrail and natural cirrus separation combining the SAC, CA and the plume detection algorithm

This section is to explain the effect of applying the plume detection algorithm on the separation of contrail and natural cirrus using SAC and CA. The N_{ice}-R_{ice} distributions for the cirrus fulfilling and not fulfilling the plume detection criteria (SAC not applied, *i.e.* SAC NA in the figures below) are plotted in Fig. S4a and c. Figure S4b and d show the corresponding RH_{ice}-T_{amb} relations. Because the plume detection depends greatly on NO_y and aerosol concentration and the enhancement signal of the species decays with time, only rather fresh plumes younger than about 4 h can be identified. Therefore, the population of cirrus particles that can be traced back to plumes is rather small, about 0.99 h sampling time, and most of the ice crystals were detected under conditions fulfilling the SAC (about 0.86 h), as shown in Fig. S4a and Fig. 5e, respectively. The difference between Fig. S4e and Fig. 5e shows that also contrails outside CA are found, which are indistinguishable from natural cirrus when only applying SAC outside CA. Temperature wise, most of the ice particles are found in the CA temperature range (207–218 K) with a high occurrence frequency in ice subsaturation, see Fig. S4 b. Most of the cirrus cannot be validated with the plume detection algorithm. They are a mixture of contrail cirrus, in situ- and liquid-origin natural cirrus, spreading in a wide temperature range, see Fig. S4c and d.

The cirrus crystals fulfilling SAC, inside CA and also with restriction to plume detection are shown in Fig. S4e, with their RH_{ice} vs. T_{amb} displayed in Fig. S4f. From Fig. S4e, we can see that the N_{ice}-R_{ice} distribution of ice particles would be represented nearly by the 50th percentile in Fig. 5e. Comparing the median N_{ice} and R_{ice} values represented by Fig. 5e and Fig. S4e (which is also listed in Table 1 in the paper), we can see that the medians in the dataset using SAC, CA and plume detection are closer to the ones determined using only the combined SAC+CA. Therefore, it does not make a big difference to add the restriction of plume detection to the combined SAC and CA criteria.
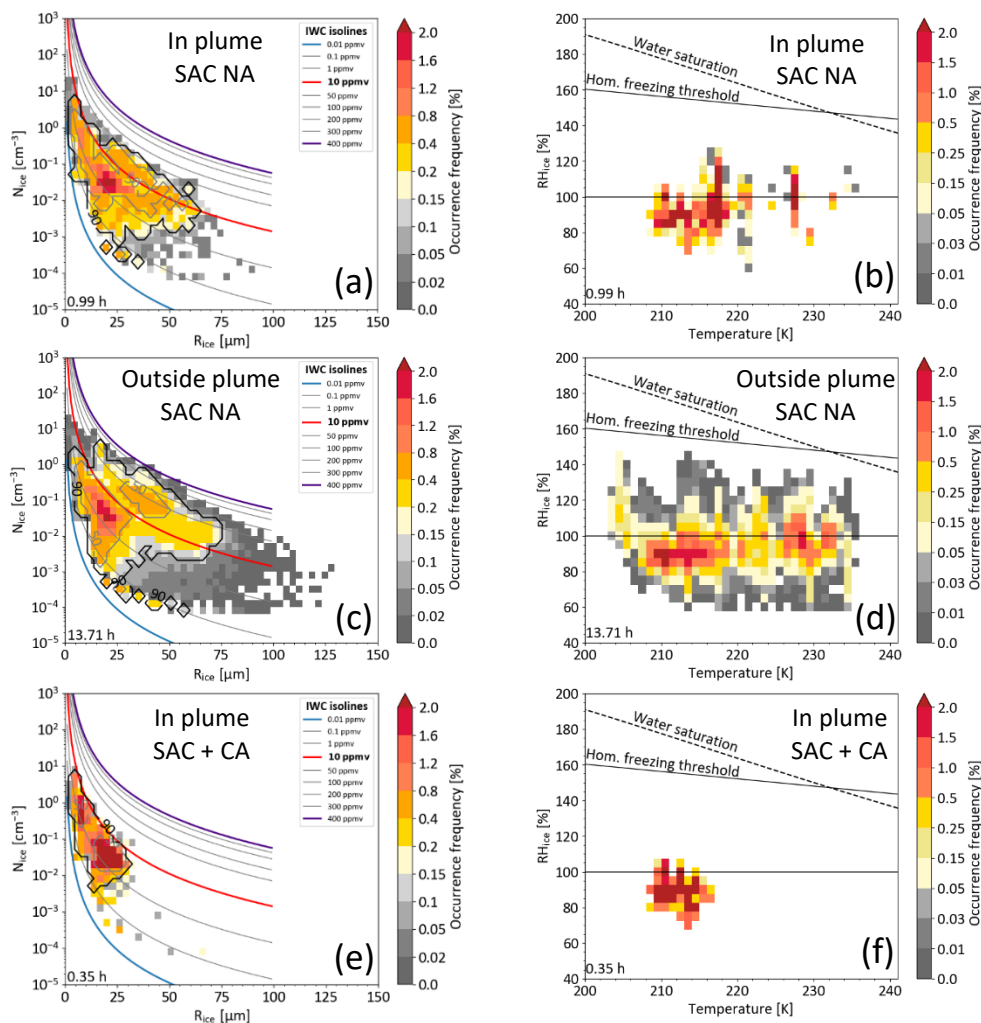
Figure S4. N_{ice}–R_{ice} relations (left) and RH_{ice}-T_{amb} relations (right) color-coded by normalised occurrence frequency, similar to Fig. 3c and d. (a): N_{ice}–R_{ice} relation for the ice particles found in aircraft plumes using the plume detection algorithm without applying the Schmidt-Appleman criterion (SAC NA) (median: N_{ice} = 0.027 cm^{-3}, R_{ice} = 23.7 µm, IWC = 5.0 ppmv and RH = 92%). (b): Corresponding RH_{ice}-
135 T_{amb} relation. (c): N_{ice}–R_{ice} relation for the cirrus outside aircraft plumes. (d): Corresponding RH_{ice}-T_{amb} relation. (e): N_{ice}–R_{ice} relation for the cirrus fulfilling the plume, SAC and CA (ambient pressure 200–245hPa) criteria (median: N_{ice} = 0.041 cm^{-3}, R_{ice} = 17.8 µm, IWC = 4.4 ppmv and RH$_{ice}$ = 89%). (f): Corresponding RH_{ice}-T_{amb} relation. See Sect. 3.2.2.1 in the paper for details.

References

Kaufmann, S., Voigt, C., Heller, R., Jurkat-Witschas, T., Krämer, M., Rolf, C., Zöger, M., Giez, A., Buchholz, B., Ebert, V.,
140 Thornberry, T., and Schumann, U.: Intercomparison of midlatitude tropospheric and lower-stratospheric water vapor measurements and comparison to ECMWF humidity data, Atmos. Chem. Phys., 18, 16729-16745, https://doi.org/10.5194/acp-18-16729-2018, 2018.

Krämer, M., Rolf, C., Spelten, N., Afchine, A., Fahey, D., Jensen, E., Khaykin, S., Kuhn, T., Lawson, P., Lykov, A., Pan, L. L., Riese, M., Rollins, A., Stroh, F., Thornberry, T., Wolf, V., Woods, S., Spichtinger, P., Quaas, J., and Sourdeval, O.: A

145 microphysics guide to cirrus – Part 2: Climatologies of clouds and humidity from observations, Atmos. Chem. Phys., 20, 12569-12608, https://doi.org/10.5194/acp-20-12569-2020, 2020.

Luebke, A. E., Afchine, A., Costa, A., Grooß, J. U., Meyer, J., Rolf, C., Spelten, N., Avallone, L. M., Baumgardner, D., and Krämer, M.: The origin of midlatitude ice clouds and the resulting influence on their microphysical properties, Atmos. Chem. Phys., 16, 5793-5809, https://doi.org/10.5194/acp-16-5793-2016, 2016.

150 Murphy, D. M. and Koop, T.: Review of the vapour pressures of ice and supercooled water for atmospheric applications, Q. J. R. Meteorol. Soc., 131, 1539-1565, https://doi.org/10.1256/qj.04.94, 2005.

Schumann, U.: On conditions for contrail formation from aircraft exhausts, Meteorol. Z., 5, 4-23, https://doi.org/10.1127/metz/5/1996/4, 1996.

Schumann, U.: Measurement and model data comparisons for the HALO-FAAM formation flight during EMeRGe on 17 July 155 2017, https://doi.org/10.5281/zenodo.4427965, 2021.

Schumann, U., Baumann, R., Baumgardner, D., Bedka, S. T., Duda, D. P., Freudenthaler, V., Gayet, J. F., Heymsfield, A. J., Minnis, P., Quante, M., Raschke, E., Schlager, H., Vázquez-Navarro, M., Voigt, C., and Wang, Z.: Properties of individual contrails: a compilation of observations and some comparisons, Atmos. Chem. Phys., 17, 403-438, https://doi.org/10.5194/acp-17-403-2017, 2017.

160 Voigt, C., Schumann, U., Minikin, A., Abdelmonem, A., Afchine, A., Borrmann, S., Boettcher, M., Buchholz, B., Bugliaro, L., Costa, A., Curtius, J., Dollner, M., Dörnbrack, A., Dreiling, V., Ebert, V., Ehrlich, A., Fix, A., Forster, L., Frank, F., Fütterer, D., Giez, A., Graf, K., Grooß, J.-U., Groß, S., Heimerl, K., Heinold, B., Hüneke, T., Järvinen, E., Jurkat, T., Kaufmann, S., Kenntner, M., Klingebiel, M., Klimach, T., Kohl, R., Krämer, M., Krisna, T. C., Luebke, A., Mayer, B., Mertes, S., Molleker, S., Petzold, A., Pfeilsticker, K., Port, M., Rapp, M., Reutter, P., Rolf, C., Rose, D., Sauer, D., Schäfler, A.,

165 Schlage, R., Schnaiter, M., Schneider, J., Spelten, N., Spichtinger, P., Stock, P., Walser, A., Weigel, R., Weinzierl, B., Wendisch, M., Werner, F., Wernli, H., Wirth, M., Zahn, A., Ziereis, H., and Zöger, M.: ML-CIRRUS: The Airborne Experiment on Natural Cirrus and Contrail Cirrus with the High-Altitude Long-Range Research Aircraft HALO, Bull. Amer. Meteor. Soc., 98, 271-288, https://doi.org/10.1175/BAMS-D-15-00213.1, 2017.